INSTITUT DE FRANCE
Académie des sciences

Comptes Rendus

Mécanique

Dimitri Goutaudier, Guillaume Osmond and Didier Gendre

Impact localization on a composite fuselage with a sparse network of accelerometers

Volume 348, issue 3 (2020), p. 191-209

Published online: 17 September 2020

https://doi.org/10.5802/crmeca.12

Les Comptes Rendus. Mécanique *sont membres du Centre Mersenne pour l'édition scientifique ouverte*
www.centre-mersenne.org
e-ISSN : 1873-7234

Comptes Rendus
Mécanique
2020, 348, nº 3, p. 191-209
https://doi.org/10.5802/crmeca.12

Impact localization on a composite fuselage with a sparse network of accelerometers

Dimitri Goutaudier[*, a, b], **Guillaume Osmond**[b] **and Didier Gendre**[c]

[a] Onera, Department of Materials and Structures, Châtillon, France

[b] Airbus, Ground Vibration Testing, Toulouse, France

[c] Airbus, Airport Operations, Blagnac, France

E-mails: dimitri.goutaudier@gmail.com (D. Goutaudier), guillaume.osmond@airbus.com (G. Osmond), didier.gendre@airbus.com (D. Gendre)

Abstract. This paper focuses on the localization of impacts applied on a composite aircraft by using low sampling frequency accelerometers. A new vibration-based approach using a modal model of the aircraft on ground is described to localize the impact on the cylindrical fuselage. Axial localization is achieved by estimating the contributions of specific vibration modes to the response. Angular localization is achieved by estimating the impact force direction. An impact test campaign is performed on an Airbus A350-900 equipped with only six accelerometers. Fifty percent of the applied impacts are localized within 2 m and more than 90% within 3 m.

Keywords. Inverse problem, Vibration analysis, Impact localization, Structural health monitoring, Composite fuselage.

Manuscript received 17th December 2019, revised and accepted 22nd April 2020.

1. Introduction

Few studies have addressed the topic of impact localization on large composite structures. Important applications are however expected from an automated structural health monitoring (SHM) technique able to cover a large area of the structure by a limited number of sensors. One example among others is the detection of ground support equipment (GSE) impacts (cargo loaders, catering vehicles, etc.) on a composite aircraft on ground at the airport. It is indeed well known [1–3] that an impact on a composite structure may produce internal damages that are invisible from a naked-eye inspection (delamination, clip disbonding, etc.). An automated SHM system could aid in reporting impact events to optimize current maintenance procedures for composite fuselages. It is therefore a strategy different from directly detecting damages by interrogating the structure using active sensors. For instance, in [4], the authors experimentally validated an SHM system able to detect damages in a large nacelle fan cowl made of composite materials.

* Corresponding author.

Many techniques have been experimentally validated under laboratory conditions on composite structures with the aim to prove their feasibility on larger structures. Some representative works known to the authors are described in the following.

Most of the existing impact localization techniques are based on a wave propagation approach. The principle is to capture the time of arrival (ToA) of some traveling waves generated by the impact at different sensor locations. The ToA delays are then used to infer the impact location by a wave propagation model. The reverse link between the ToA delays and the impact location is called triangulation in the following.

Zhao *et al.* [5] used the antisymmetric Lamb wave mode A_0 [6] to triangulate an impact event on a 400 mm × 400 mm carbon fiber reinforced polymer (CFRP) plate by using four strain gauges at a sampling frequency of 1 MHz. They solved a nonlinear triangulation problem depending on wave propagation angles by a hybrid minimization procedure based on a particle swarm optimization algorithm and a genetic algorithm. Seydel *et al.* [7] solved the triangulation problem by minimizing the quadratic distance between the ToAs predicted by a finite element model of the structure and the ToAs extracted from the measurements. They validated their technique on a 584 mm × 610 mm stiffened composite panel manufactured by Boeing equipped with four PZT sensors at a sampling frequency of 100 kHz.

Instead of using a wave propagation model that may not correctly represent the actual behavior of the propagation media, a reference database, or baseline, can be used. The first step is to record offline the sensor measurements due to impacts applied at various locations on the structure. Then, in the case of an online impact event, the sensor measurements are compared to the baseline to infer the impact location. Frieden *et al.* [8] validated such a technique on a 300 mm × 300 mm CFRP plate equipped with four FBG sensors at a sampling frequency of 1 GHz. They captured the ToAs of the A_0 Lamb wave mode to intersect iso-propagation lines derived from their reference database. Shrestha *et al.* [9] proposed the computation of correlation coefficients between the measured signals and the reference signals. They verified their approach on a 1:1 scale composite wing of a Jabiru aircraft equipped with six FBG sensors distributed along a line at a sampling frequency of 100 kHz.

Methods based on artificial neural networks (ANNs) have also been developed to triangulate the impact location from the ToA delays without any assumption on the propagation media. The ANNs are mathematical models that can be trained with a reference data set to model a nonlinear relationship between inputs and outputs. Zhong *et al.* [10] used an ANN trained with 50 reference impact tests to detect impacts on a 1040 mm × 1820 mm stiffened composite panel. The inputs of the ANN were the measurements of 10 PZT sensors at a sampling frequency of 2 MHz and the outputs were the impact location and the impact energy. Seno *et al.* [11] also developed an ANN using the ToA delays, and they demonstrated its robustness with respect to varying operational conditions (ambient vibration noise, impactor properties, and temperature). They applied their technique to a 290 mm × 285 mm curved composite panel equipped with six PZT sensors at a sampling frequency of 2 MHz.

Many other techniques have been proposed to localize an impact from vibration measurements. The linear inverse problem of impact force reconstruction can be solved by moving the candidate impact location [12–14]; the time reversal approach can be employed [15,16]; the maximum of the power signal distribution can be computed [17]; and various statistical methods have been developed [18–20].

In the case of a GSE impact on a composite fuselage, complex wave propagation phenomena are expected to occur such as wave dispersion, scattering, reflection, and attenuation. With the above-mentioned wave-based approaches, it would be necessary to significantly increase the number of sensors so that such phenomena would be negligible within each cell of the refined sensor network.

The impact localization methodology proposed in this paper is an attempt to circumvent both the scientific and the technical obstacles from classical triangulation techniques. In particular, the proposed methodology works with a low number of low sampling frequency accelerometers (200 Hz). The concession is to lower the expectations regarding the localization accuracy, which approximately reaches 4% of the aircraft length.

The technique presented in this paper was initially published in [21], but it was experimentally validated on a small metallic plate under laboratory conditions. The two main contributions of this paper are to validate the proposed technique on a very large industrial composite structure and to demonstrate that a few low frequency sensors may be sufficient to localize impacts with good accuracy.

This paper is organized as follows. Section 2 introduces the theoretical framework of the proposed impact localization technique. Section 3 describes the numerical implementation of the proposed approach. Finally, Section 4 presents the results of an impact test campaign on an Airbus A350-900.

2. Theory: cylindrical localization from a 1D modal model of an aircraft on ground

Consider a cylindrical aircraft fuselage, initially at rest, subjected to an impact at time $t = t_0$ on point $F = (x, \theta)$ with a force vector normal to the surface (transverse impact). This situation is depicted in Figure 1. The impact energy is assumed high enough to produce a global vibration response of the complete aircraft. Consequently, the vibration response $q(t)$, measured at any point C on the fuselage along the Y-direction or the Z-direction, is not null and can be divided into three distinct regions:

- $t \in [t_0, t_1]$: Rest—the elastic waves generated by the impact have not reached the sensor location yet.
- $t \in [t_1, t_2]$: Wave passages—some waves reach the sensor location C and keep traveling through the structure.
- $t \geq t_2$: Modal behavior—the waves of sufficient energy superimpose into global vibration modes of the aircraft until complete attenuation is achieved.

A more comprehensive description of these phases can be found in [22]. Classical triangulation techniques in the time domain capture the frontier between the first two phases by identifying t_1, commonly called the time of arrival, at different sensor locations. A wave propagation model is then used to infer the impact location from the captured ToAs. However, these methods become challenging for an aircraft fuselage because of the various complex wave propagation phenomena that may occur (dispersion, scattering, reflection on stiffeners, etc.). In addition, the frequencies of the participating traveling waves are very high and require expensive high sampling frequency sensors for their capture.

As an alternative, it is proposed in Section 2.2 to take advantage of the low-frequency content of the modal superposition phase to localize the axial coordinate x of the impact point. The angular coordinate θ is captured by another strategy described in Section 2.3 based on the identification of the force vector direction.

2.1. *Low-frequency modal behavior description*

Let us denote by $\phi_j^{(d)}(M)$ the jth mass-normalized mode shape of the structure evaluated at some point M on the fuselage along direction d. The measurement direction is denoted as m (either along the Y-axis or the Z-axis in this study) and the impact direction is denoted as n

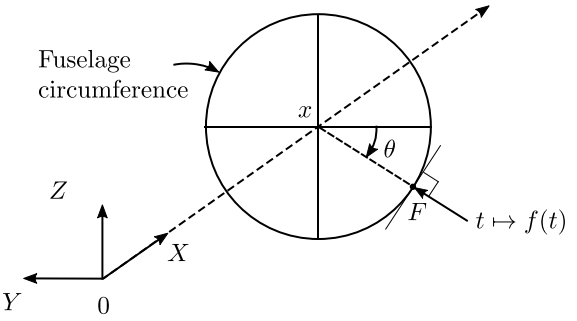

Figure 1. Localization of a transverse impact on cylindrical fuselage (aircraft axis X oriented from front to rear).

(normal to the surface). The governing equation of the modal superposition phase, measured in displacements at point C and due to a transverse impact at point F, is given by [23]

$$\tilde{q}^{(m)}(t) = \sum_{j=1}^{p} \phi_j^{(m)}(C)\phi_j^{(n)}(F)(f * g_j)(t). \tag{1}$$

The superscript $\tilde{\cdot}$ indicates that model (1) is only valid within the frequency band of the considered p vibration modes, and $(f * g_j)(t)$ represents the convolution product between the applied load history $f(t)$ and the jth modal impulse response $g_j(t)$. The latter is given by

$$g_j(t) = \frac{1}{\omega_j} \mathrm{e}^{-\eta_j \omega_{0j} t} \sin(\omega_j t), \tag{2}$$

where $\omega_{0j} > 0$ and $\eta_j < 1$ are, respectively, the natural pulsation and the damping ratio of the jth mode and where $\omega_j = \omega_{0j}\sqrt{1-\eta_j^2}$.

In this study, only low-frequency vibration modes of the aircraft are considered (natural frequency lower than 15 Hz) so that the impact load history is assumed to be a Dirac function with intensity f_δ (expressed in N·s). Consequently, $(f * g_j)(t) = f_\delta g_j(t - t_0)$, and the acceleration response model $\tilde{a}^{(m)}(t)$ is given by

$$\tilde{a}^{(m)}(t) = \begin{cases} \sum_{j=1}^{p} \phi_j^{(m)}(C)\phi_j^{(n)}(F) f_\delta \ddot{g}_j(t - t_0) & \text{if } t \geq t_0 \\ 0 & \text{if } t < t_0. \end{cases} \tag{3}$$

Note that only acceleration measurements are considered in this study since accelerometers are small sensors that do not require a reference point. Note also that the modal superposition phase is assumed to start from t_0 instead of a certain time $t_2 \geq t_0$.

2.2. *Axial localization*

Without any loss of generality, let us assume that both the measurement direction and the impact direction are along the Y-axis to avoid using superscripts ($m = n = Y$). By reordering the terms in (3), the acceleration response model for $t \geq t_0$ can be written as

$$\tilde{a}(t) = \ddot{\mathbf{L}}(t, t_0) \cdot \mathbf{Z_F}, \tag{4}$$

where $\ddot{\mathbf{L}}(t, t_0)$ and $\mathbf{Z_F}$ are defined by

$$\ddot{\mathbf{L}}(t, t_0) = (\phi_1(C)\ddot{g}_1(t - t_0) \cdots \phi_p(C)\ddot{g}_p(t - t_0)) \tag{5}$$

$$\mathbf{Z_F} = f_\delta \cdot (\phi_1(F) \cdots \phi_p(F))^T. \tag{6}$$

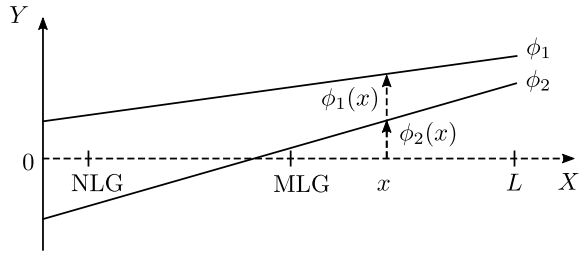

Figure 2. Pitch and heave modes of an aircraft on ground (beam model with NLG = nose landing gear, MLG = main landing gear, and L = aircraft length). The ratio $\phi_2(x)/\phi_1(x)$ is a signature of the axial coordinate x of the impact point F.

In the following, the terms $\phi_j(F)$ are called modal ponderations. If the impact occurs at the modal node of the ith mode, then the ith mode will not participate in the response (null ponderation: $\phi_i(F) = 0$). It can be noted that the impact intensity f_δ does not change the proportions in which the vibration modes are excited. It is actually proved in [21] that $\mathbf{Z_F}$ is bijectively linked to the impact point:

$$\mathbf{Z_F} \leftrightarrow F \tag{7}$$

if appropriate vibration modes are selected in the analysis. It is also evidenced in [21] that the identification of $\mathbf{Z_F}$ (presented in Section 3.3) is quite sensitive to the sensor locations. In particular, the sensors must not be located on a modal node of one of the modes considered in the analysis; otherwise, the corresponding modal ponderation cannot be sensed.

The physical idea behind relation (7) is that the proportions in which specific vibration modes are excited depending on the impact location are unique. Consequently, the vector $\mathbf{Z_F}$ can be seen as a signature of the impact point F in the vibration response. A procedure is presented in Section 3.3 to estimate the unknowns $\mathbf{Z_F}$ and t_0 from acceleration measurements.

To understand how a list of modal ponderations may connect to the impact point, let us consider the transverse vibrations in the $(0XY)$ plane of an aircraft on ground undergoing an impact of intensity $f_\delta \neq 0$ with axial coordinate x. Let us denote by ϕ_1 and ϕ_2 the heave and the pitch mode shapes of the aircraft, respectively, so that $\mathbf{Z_F} = f_\delta \cdot (\phi_1(x)\ \phi_2(x))^T$ with

$$\phi_1(x) = ax + b \quad \phi_2(x) = cx + d, \tag{8}$$

where $ab > 0$ and $cd < 0$ (see Figure 2). The proportion $\lambda(x)$ of the pitch mode with respect to the heave mode in the vibration response is given by the ratio of the two coordinates of $\mathbf{Z_F}$:

$$\lambda(x) = \frac{\phi_2(x)}{\phi_1(x)} = \frac{cx + d}{ax + b}. \tag{9}$$

A basic study of the function $\lambda : x \mapsto \lambda(x)$ shows that λ is injective (under the conditions $ab > 0$ and $cd < 0$). Hence the proportion of these two modes is uniquely linked to the axial coordinate x of the impact point. Therefore, λ can be inverted to obtain x from the knowledge of $\lambda(x)$.

More generally, the procedure described in Section 3.1 is used to create the reverse link $\mathbf{Z_F} \mapsto F$. The key point is to use a family of vibration modes so that mapping (7) is valid. Such a family is called a discriminating mode family (DMF). A procedure is given in Section 3.2 to identify DMFs of an aircraft from an experimental modal analysis (EMA).

2.3. *Angular localization*

In theory, the localization technique presented in Section 2.2 could be used for capturing the angular coordinate θ of the impact point. It would require the consideration of ovalization vibration

modes of the fuselage ($\phi_j(x,\theta)$ depending on θ for a given axial coordinate x). However, these vibration modes are difficult to identify experimentally even during dedicated ground vibration tests (GVT) as a GVT usually captures rigid and bending fuselage modes of an aircraft [24].

As an alternative, it is proposed to estimate the impact force direction (assumed to be normal to the fuselage). It can be seen in Figure 1 that the angular coordinate θ of the impact point is linked to the impact force direction $\mathbf{f} = (f_Y \ f_Z)$ through the following relation (provided that $f_Y \neq 0$):

$$\tan(\theta) = \frac{f_Z}{f_Y}. \tag{10}$$

The objective is then to identify f_Y and f_Z from vibration measurements in the Y-direction and the Z-direction. However, relation (3) exhibits a direction coupling: an impact applied along the Y-axis may produce a vibration response along the Z-axis. This difficulty can be solved by considering a frequency band over which the vibration modes are purely planar. This will be precisely the case between 3 Hz and 11 Hz for the aircraft we will be dealing with in Section 4. In such a frequency band, the acceleration response in the Y-direction (respectively, in the Z-direction) is uniquely linked to the Y-component (respectively, the Z-component) of the impact force:

$$\tilde{a}^{(Y)}(t) = \sum_{j=1}^{p} \phi_j^{(Y)}(C)\phi_j^{(Y)}(F) f_Y \ddot{g}_j(t-t_0), \tag{11}$$

$$\tilde{a}^{(Z)}(t) = \sum_{j=1}^{p} \phi_j^{(Z)}(C)\phi_j^{(Z)}(F) f_Z \ddot{g}_j(t-t_0). \tag{12}$$

The procedure described in Section 3.3 is then used to identify f_Y from acceleration measurements along the Y-axis and f_Z from acceleration measurements along the Z-axis. Relation (10) then provides the angular coordinate θ of the impact point.

3. Implementation: estimation of modal ponderations and impact direction from acceleration measurements

The proposed strategy consists of the following steps:

- identification of DMFs from a modal analysis of the structure;
- estimation of the unknowns $\mathbf{Z_F}$ and t_0 from acceleration measurements;
- reverse link $\mathbf{Z_F} \mapsto F = (x,\theta)$.

The implementation of this methodology is described for the tested aircraft in Section 4. The proposed procedure is however general, and the flowchart presented in Section 3.4 could fit other structures.

The reverse link is presented before the other two steps for the following reasons. First, the DMF identification step cannot be understood prior to an explanation on how the reverse link is performed. Second, it is intended to highlight how simple it is to retrieve the impact location from a list of modal ponderations rather than solving a nonlinear triangulation problem.

3.1. *Reverse link*

The required input for the proposed impact localization methodology is a modal analysis of the structure. The modal analysis can be performed either numerically or experimentally depending on the available information. For the aircraft, an EMA has been performed prior to the impact tests by the ground vibration testing team of Airbus. The results of this EMA are presented in the Appendix. It is however beyond the scope of this paper to present the existing EMA techniques. The reader is invited to find more details on this topic from [25].

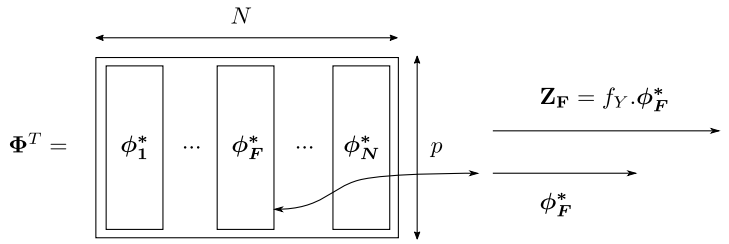

Figure 3. Illustration of the collinearity research procedure with a modal matrix truncated on a DMF.

The mode shapes of the aircraft have been evaluated along the Y-axis and the Z-axis, but the reverse link is presented here (without loss of generality) by considering the Y-components only. Let us consider $\phi_j(M)$, the jth mass-normalized mode shape evaluated at some point M along the Y-axis. The evaluation points of the mode shapes are called degrees of freedom (DOF) in the following. Let p be the number of known vibration modes and N be the number of DOFs. Therefore, an $N \times p$ modal matrix $\mathbf{\Phi}$ is available. Let $\boldsymbol{\phi}_\mathbf{i}^*$ be the columns of $\mathbf{\Phi}^T$ so that

$$\mathbf{\Phi}^T = [\boldsymbol{\phi}_\mathbf{1}^* | \cdots | \boldsymbol{\phi}_\mathbf{N}^*]. \tag{13}$$

Assuming that the impact point is among the N points at which the mode shapes have been evaluated, let $F \in [\![1, N]\!]$ be the index of the associated DOF. The vector $\mathbf{Z_F}$ is then given by

$$\mathbf{Z_F} = f_Y \cdot \boldsymbol{\phi}_\mathbf{F}^*, \tag{14}$$

where $f_Y \neq 0$ is the impact intensity along the Y-axis.

Relation (14) shows that the index F of the impacted DOF is among the indices $i \in I \subset [\![1, N]\!]$ so that $\boldsymbol{\phi}_\mathbf{i}^*$ and $\mathbf{Z_F}$ are collinear. Therefore, a simple collinearity search procedure between $\mathbf{Z_F}$ and the columns of $\mathbf{\Phi}^T$ evidences a set of candidate points, denoted by $\mathscr{C}(\mathbf{Z_F})$ in the following, with the impact point being part of it:

$$F \in \mathscr{C}(\mathbf{Z_F}). \tag{15}$$

The impact localization problem is then well posed (unique solution) if $\mathscr{C}(\mathbf{Z_F}) = \{F\}$. This occurs if the modal matrix $\mathbf{\Phi}$ is truncated over specific vibration modes (see Section 3.2). Under this condition, the impact point F is retrieved by looking for the unique column of $\mathbf{\Phi}^T$ collinear to $\mathbf{Z_F}$ (see Figure 3). The collinearity factor is nothing but the impact intensity f_Y.

3.2. *DMF identification*

The objective is to identify the vibration mode families so that the bijective mapping (7) is valid. Note that this mapping must be valid for each point of the structure that could be impacted since the impact location is unknown prior to the selection of a vibration mode family. Such a selection of vibration modes is called a discriminating mode family.

Influence of uncertainties

It is proposed in Section 3.1 to achieve the reverse link between $\mathbf{Z_F}$ and F by a simple collinearity research procedure. Therefore, a DMF could be identified solely by checking whether the columns of $\mathbf{\Phi}^T$ are two-by-two independent ($\phi_i^* = \alpha\phi_j^* \Rightarrow i = j$). In this way, an exact estimation of $\mathbf{Z_F}$ would lead to an exact identification of both the impact location and the impact intensity (provided that the impact point is among those at which the mode shapes have been evaluated).

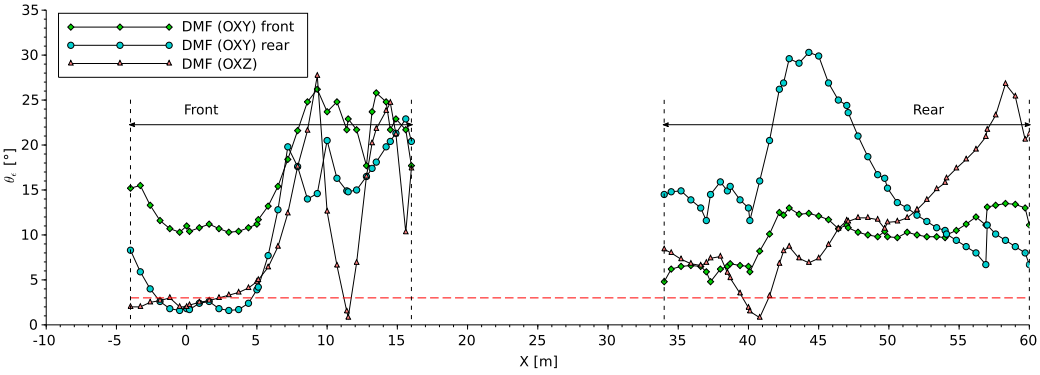

Figure 4. Selected DMFs based on the angular robustness maps computed with $\epsilon = 3$ m, $\theta_0 = 1°$, and $\Delta\theta = 0.1°$. In the $(0XY)$-plane, the family $(\phi_7, \phi_9, \phi_{11})$ is used for the front half and $(\phi_3, \phi_5, \phi_{11})$ is used for the rear half (higher values of θ_ϵ). The best family found in the $(0XZ)$-plane with the available modes is $(\phi_6, \phi_8, \phi_{10})$ even if θ_ϵ does not exceed the threshold of 3° at some DOFs.

However, the difficulty is to take into account the inaccuracy on both the modal analysis (input error) and the vector $\hat{\mathbf{Z}}_\mathbf{F}$ estimated as per the procedure in Section 3.3 (output error). The estimation error on $\mathbf{Z}_\mathbf{F}$ may be a consequence of mode shapes not being evaluated at point F, or model errors according to the modal behavior assumption, or of measurement noise. Consequently, $\hat{\mathbf{Z}}_\mathbf{F}$ might not be exactly collinear to $\boldsymbol{\phi}_\mathbf{F}^*$.

Angular Robustness Maps

The idea proposed in [21] is to concede localizing the impact point within a proximity tolerance $\epsilon > 0$, which results in introducing a collinearity tolerance into the procedure. More precisely, let us denote as $S = \{M_1, \ldots, M_N\}$ the points of the structure attached to the evaluated DOFs and let us denote as $\theta \in [0, \pi/2[$ a collinearity tolerance angle. Now, let us introduce the following definitions:

- $\mathscr{B}(M_i, \epsilon) \subset S$, the set of points $M_j \in S$ that are ϵ-close to the point M_i;
- $\mathscr{C}(\boldsymbol{\phi}_\mathbf{i}^*, \theta) \subset S$, the set of points $M_j \in S$ such that the associated $\boldsymbol{\phi}_\mathbf{j}^*$ makes an angle with $\text{span}(\boldsymbol{\phi}_\mathbf{i}^*)$ lower than θ.

A collinearity tolerance angle θ is said to be admissible for the point $M_i \in S$ (and for the selected proximity tolerance ϵ) if the associated $\boldsymbol{\phi}_\mathbf{i}^*$ satisfies

$$\mathscr{C}(\boldsymbol{\phi}_\mathbf{i}^*, \theta) \subset \mathscr{B}(M_i, \epsilon). \tag{16}$$

The maximum admissible collinearity tolerance angle for the point M_i is denoted by $\theta_\epsilon(M_i)$ in the following. The DMF identification consists in plotting

$$M_i \mapsto \theta_\epsilon(M_i) \tag{17}$$

for each $M_i \in S$ and for different combinations of vibration modes. Such a plot is called an angular robustness map (ARM). The vibration mode families such that θ_ϵ is greater than 3°–4° are considered as candidate DMFs. In practice, $\theta_\epsilon(M_i)$ is computed by starting with an initial collinearity tolerance θ_0 and by increasing it by $\Delta\theta$ until relation (16) is not valid. Figure 4 shows the ARMs of the DMFs selected for the studied aircraft. Note that the fuselage section between 16 m and 34 m is not considered as an impact area (see Section 4.2).

3.3. *Model identification*

The unknowns of the acceleration response model (3) are the impact time t_0, the impact location $F = (x,\theta)$ on the fuselage, and the impact intensity f_δ. As proposed in Section 2.3, we shall consider the acceleration measurements within a frequency band over which the vibration modes are purely planar, either in the (OXY)-plane or in the (OXZ)-plane. This condition is verified for the aircraft in the range 3 Hz–11 Hz (see Appendix). Therefore, two models are to be identified, one for each measurement direction:

$$\tilde{a}^{(Y)}(t) = \ddot{\mathbf{L}}^{(Y)}(t,t_0)\cdot\mathbf{Z}_{\mathbf{F}}^{(Y)}, \tag{18}$$

$$\tilde{a}^{(Z)}(t) = \ddot{\mathbf{L}}^{(Z)}(t,t_0)\cdot\mathbf{Z}_{\mathbf{F}}^{(Z)}. \tag{19}$$

A reverse link, introduced in Section 3.1 and presented in its final form in Section 3.4, is then used to identify x, f_Y and f_Z from the estimations of the vectors $\mathbf{Z}_{\mathbf{F}}^{(Y)}$ and $\mathbf{Z}_{\mathbf{F}}^{(Z)}$. Then relation (10) provides the angle θ from f_Y and f_Z.

The model identification methodology consists of two sequential steps, a rough estimation followed by a refinement, using the measurements of two sensor networks. Note that some sensors might belong to both networks.

Secondary sensor network

The purpose of the secondary sensor network is to provide a coarse localization of the impacted zone and a rough estimation of the impact time. It is however not the purpose of this paper to discuss the optimization and the design of the secondary sensor network. There is already an extensive literature on sensor networks able to perform such tasks [26].

A network of six single-axis accelerometers measuring vibrations in the Y-direction has been used (three in the front part and three in the rear part). The sampling frequency of these accelerometers is 200 Hz. This secondary sensor network is able to detect which half of the aircraft has been impacted (front or rear). This detection is achieved by determining the sensor responding first. The instant

$$t = \tau \tag{20}$$

at which the first sensor reaches its maximum signal magnitude is used as a rough estimation of the impact time (it is actually an upper bound: $t_0 \leq \tau$). This approximation is based on the observation that an impact response mainly consists of a decaying oscillatory response (see Section 4.2).

Primary sensor network

The purpose of the primary sensor network is to provide the appropriate measurements to refine the estimation of the impact time t_0 and to estimate the vectors $\mathbf{Z}_{\mathbf{F}}^{(Y)}$ and $\mathbf{Z}_{\mathbf{F}}^{(Z)}$. This is achieved through a minimization procedure described below. The objective function to be minimized is a quadratic distance between the measurements and the model predictions. After the resolution of this optimization problem, the impact location is retrieved by using the technique presented in Section 2.

The two sensor networks used for the aircraft are depicted in Figure 5. All the sensors have been installed along a line of the aircraft belly according to the 1D modal model built during the EMA. The measurement axes of the secondary sensors are displayed in purple and those of the primary sensors are displayed in red. Either the front or the rear couple of primary sensors is selected for the model identification step depending on the detection of the impacted half. Priority is given to the so-called master sensor to provide the estimation of the axial coordinate of the impact point.

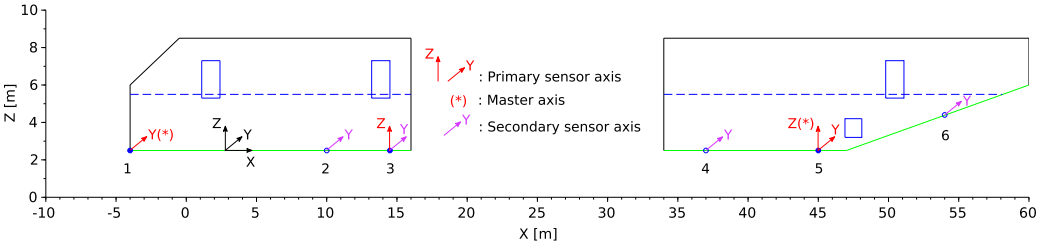

Figure 5. Primary and secondary sensor networks used for the studied aircraft (bi-axis accelerometers from PCB Piezotronics, 356A14, with a sampling frequency of 200 Hz).

Note that the sensor locations have a great influence on the quality of model identification. An analysis is given in [27] providing optimal sensor locations according to the selected DMFs.

Minimization procedure

The objective function to be minimized with the measurements along the Y-axis and the Z-axis of the two primary sensors of the impacted half is

$$J(t_0, \mathbf{Z_F}) = \sum_{i=1}^{n} (\ddot{\mathbf{L}}(t_i, t_0) \cdot \mathbf{Z_F} - a(t_i))^2. \tag{21}$$

To do so, pre-defined values of the impact time are tested:

$$t_0^{(k)} = \tau - k/f_s, \tag{22}$$

where f_s is the sampling frequency of the primary network (200 Hz for the studied aircraft) and k is a positive integer. The maximum value of k is set according to the maximum traveling time of the waves between each extremity of the aircraft (30 ms for the studied aircraft).

The minimization of (21) with a pre-defined value of t_0 is a well-known linear least-squares problem. The couple $(\hat{t}_0, \hat{\mathbf{Z}}_\mathbf{F})$ minimizing the objective function is selected as the solution.

Model (4) could be identified with a strategy other than a standard linear least-squares procedure. However, with the formalism presented in this paper, the identification of $\mathbf{Z_F}$ from the measurements $a(t_i)$ only consists in solving an overdetermined linear system. The least-squares method is attractive for solving it with a unique solution in real time and with sufficient robustness properties for this application.

3.4. *Final procedure*

The program flowchart is given in Figure 6. The different steps of this procedure were implemented using Scilab 5.5.2. The raw measurements were low-pass-filtered to remove irrelevant high-frequency noise (second-order Butterworth filter with a 50 Hz cutoff frequency). The signals were also time-windowed to obtain an acquisition duration of 5 s.

The reverse link $\hat{\mathbf{Z}}_\mathbf{F} \mapsto (\hat{x}, \hat{f})$ is performed in the final procedure as follows:

- Determine $S_1 = \mathscr{C}(\hat{\mathbf{Z}}_\mathbf{F}, \pi/4)$ as the first set of impact point candidates (see notation in Section 3.2).
- Determine $\theta_{\min}$, the minimum angle between span$(\hat{\mathbf{Z}}_\mathbf{F})$ and the $\boldsymbol{\phi}_\mathbf{i}^*$ associated with the candidates $M_i \in S_1$.
- Determine $S_2 = \mathscr{C}(\hat{\mathbf{Z}}_\mathbf{F}, \gamma \cdot \theta_{\min}) \cap S_1$, where $\gamma \geq 1$ is a pre-selected dispersion factor.
- Compute the axial coordinate of the impact point as follows:

$$\hat{x} = \sum_i w_i x_i, \tag{23}$$

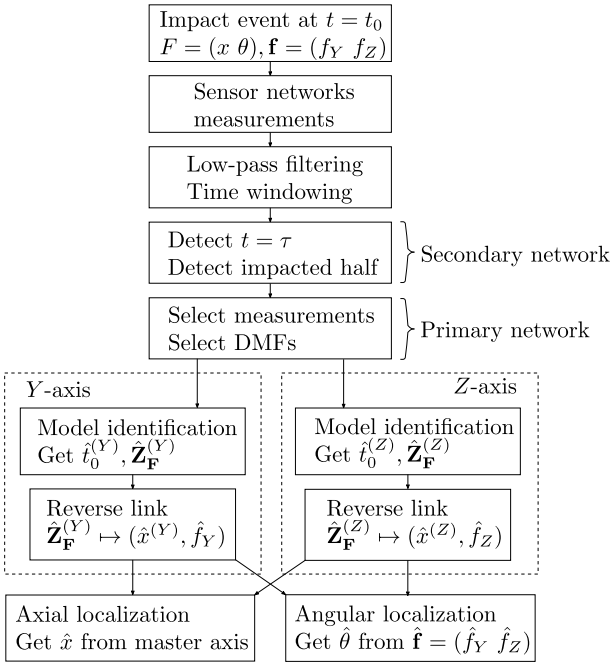

Figure 6. Program flowchart of the impact localization technique.

where the x_i are the axial coordinates of the points $M_i \in S_2$ and the w_i are weighting factors. These latter are given by $w_i = \cos(\hat{\theta}_i) / \sum_k \cos(\hat{\theta}_k)$, where $\hat{\theta}_i$ is the angle between span($\hat{\mathbf{Z}}_{\mathbf{F}}$) and the $\boldsymbol{\phi}_{\mathbf{i}}^*$ associated with the candidate $M_i \in S_2$.

- Compute the intensity of the impact as follows:

$$\hat{f} = \sum_i w_i f_i, \tag{24}$$

where the w_i are the same weighting factors as in (23) and the f_i are the collinearity factors between the $\boldsymbol{\phi}_{\mathbf{i}}^*$ associated with the points $M_i \in S_2$ and $\hat{\mathbf{Z}}_{\mathbf{F}}$:

$$f_i = \frac{(\boldsymbol{\phi}_{\mathbf{i}}^*)^T \cdot \hat{\mathbf{Z}}_{\mathbf{F}}}{\|\boldsymbol{\phi}_{\mathbf{i}}^*\|_2^2}. \tag{25}$$

The motivation for this collinearity research procedure is described in the following. As illustrated in Figure 4, there might be important discrepancies in the values of $\theta_e(F)$ depending on the impact location F. Consequently, an adaptive collinearity tolerance must be employed. The first set of impact point candidates is identified by determining the $\boldsymbol{\phi}_{\mathbf{i}}^*$ that are roughly collinear to the estimated vector $\hat{\mathbf{Z}}_{\mathbf{F}}$ (angles less than $\pi/4$). Then this set is refined by selecting only the candidates M_i associated with the $\boldsymbol{\phi}_{\mathbf{i}}^*$ that are most collinear to $\hat{\mathbf{Z}}_{\mathbf{F}}$ according to a dispersion factor γ ($\gamma = 2$ was selected for the studied aircraft).

Note that the sensitivity of γ to the localization results is low if $\theta_{\min} \approx 0$, meaning that there is a strong confidence in one candidate. If not, the intersection of $\mathscr{C}(\hat{\mathbf{Z}}_{\mathbf{F}}, \gamma \cdot \theta_{\min})$ with S_1 prevents selecting candidates associated with $\boldsymbol{\phi}_{\mathbf{i}}^*$ that are far from being collinear with $\hat{\mathbf{Z}}_{\mathbf{F}}$.

The axial coordinate of the impact point and the impact intensity are then estimated by the barycenter technique (Equations (23)–(24)). The latter gives more weight to candidates associated with the $\boldsymbol{\phi}_{\mathbf{i}}^*$ that are the most collinear to $\hat{\mathbf{Z}}_{\mathbf{F}}$.

Figure 7. (a) Tested aircraft (A350-900 MSN003). (b) Impact locations around the rear passenger door. (c) Impact hammer.

4. Experiments: results of an outdoor impact test campaign on an Airbus A350-900

The two main objectives of this section are as follows:

- Demonstrate the applicability of the proposed impact localization technique on a 1:1 scale composite aircraft under outdoor conditions. Note that this technique has been previously validated under laboratory conditions on metallic and composite structures of much smaller dimensions in [27].
- Present a technical architecture of this methodology with a sparse network of low sampling frequency sensors. As mentioned in Section 2, classical impact localization techniques based on wave propagation would require an expensive dense network of high sampling frequency sensors.

It is however not the purpose of this paper to provide an optimal configuration of the sensor networks (sensor locations, type of sensors, measurement parameters, etc.). Indeed the time to perform these tests, including the EMA, has limited our number of trials.

4.1. *Setup*

The aircraft is an Airbus A350-900 on ground without engines (see Figure 7). It is not in flight configuration any longer and is dedicated to "lab tests." As any other A350 aircraft, the fuselage skin and the main components of the structure (stringers in the axial direction and frames in the radial direction) are made of composite materials.

The aircraft has been impacted on the external skin of the fuselage by a 5.5 kg hand-held impact hammer from PCB Piezotronics, 086D50. Therefore the applied impacts during these tests have a much lower energy than the GSE impacts that may occur during the operational life of an aircraft [28]. In addition, it has been observed that the vibrations induced by the impact hammer did not propagate well from one end of the aircraft to the other end (strong signal attenuation). This is why the secondary network presented in Section 3.3 is dedicated to the detection of which half has been impacted (front or rear). The primary sensor measurements for the model identification step are then selected in accordance with the impacted half. Figure 5 presents the sensor network configuration used for these tests. Table 1 summarizes both the measurement

Table 1. Properties of the tested aircraft and selected measurement and methodology parameters

Aircraft	Length: 65 m Fuselage: composite skin, composite stiffeners
Sensors	Six bi-axis accelerometers from PCB Piezotronics, 356A14 distributed along a line of the aircraft belly Measurement axes: Y and Z Sampling frequency: 200 Hz Acquisition duration: 5 s
Acquisition system	Data Physics ABACUS LMS Test Lab 15A
Methodology parameters	DMF (OXY) front half: $\phi_7, \phi_9, \phi_{11}$ DMF (OXY) rear half: $\phi_3, \phi_5, \phi_{11}$ DMF (OXZ) front and rear: $\phi_6, \phi_8, \phi_{10}$ Dispersion factor: $\gamma = 2$

and the methodology parameters. All the sensors are glued to the exterior skin of the fuselage to ease their installation for the tests.

4.2. *Localization maps*

The impacts have been applied at 23 different locations according to a typical distribution of impacts on a fuselage during its operational life [29]. The impact locations are mainly concentrated around the passenger and cargo doors on the lower half of the fuselage. For simplicity during the tests, all the impacts have been applied on the left side of the aircraft. No impact has been applied on the central section of the fuselage (between 16 m and 34 m), which is obstructed by the wings of the aircraft. In addition, all the impacts have been applied thrice per location to test both the accuracy and the robustness of the proposed impact localization method. These two aspects are discussed in Section 4.3.

Figure 8 illustrates the different steps of a single impact localization for an impact applied on the bottom/right of the rear passenger door. As described in the flowchart presented in Figure 6, all the measurements of the secondary networks are used to determine the sensor responding first. In the present case, the latter is the rear sensor 6Y (see Figure 5) and hence the detected half is the rear. The measurements of the rear primary sensors (5Y and 5Z) are then used for the model identification step. The spectrum reconstruction of the measured acceleration signal 5Z is presented to illustrate that the contributions of the DMF modes in the (OXZ)-plane have been correctly captured (reconstruction of the blue curve within the DMF bandwidth).

Figure 9 presents the localization maps of the three series of impacts. The red cross represents an actual impact location and the black cross represents an estimated location. Note that the Z-coordinate of the impact point is derived from the angular coordinate θ estimated by the technique presented in Section 2.3. Table 2 summarizes the mean 1D localization errors in the X-direction or in the Z-direction and the mean 2D localization error.

First, it can be appreciated that 100% of the applied impacts are detected by only six accelerometers (no stand-alone red crosses). Hence the contributions of the DMF modes are correctly extracted from the measured vibration responses even if the number of excited vibration modes is high. In particular, it can be seen in Figure 8 that the reconstructed frequency band is typically small with respect to the actual frequency content of the measured signal.

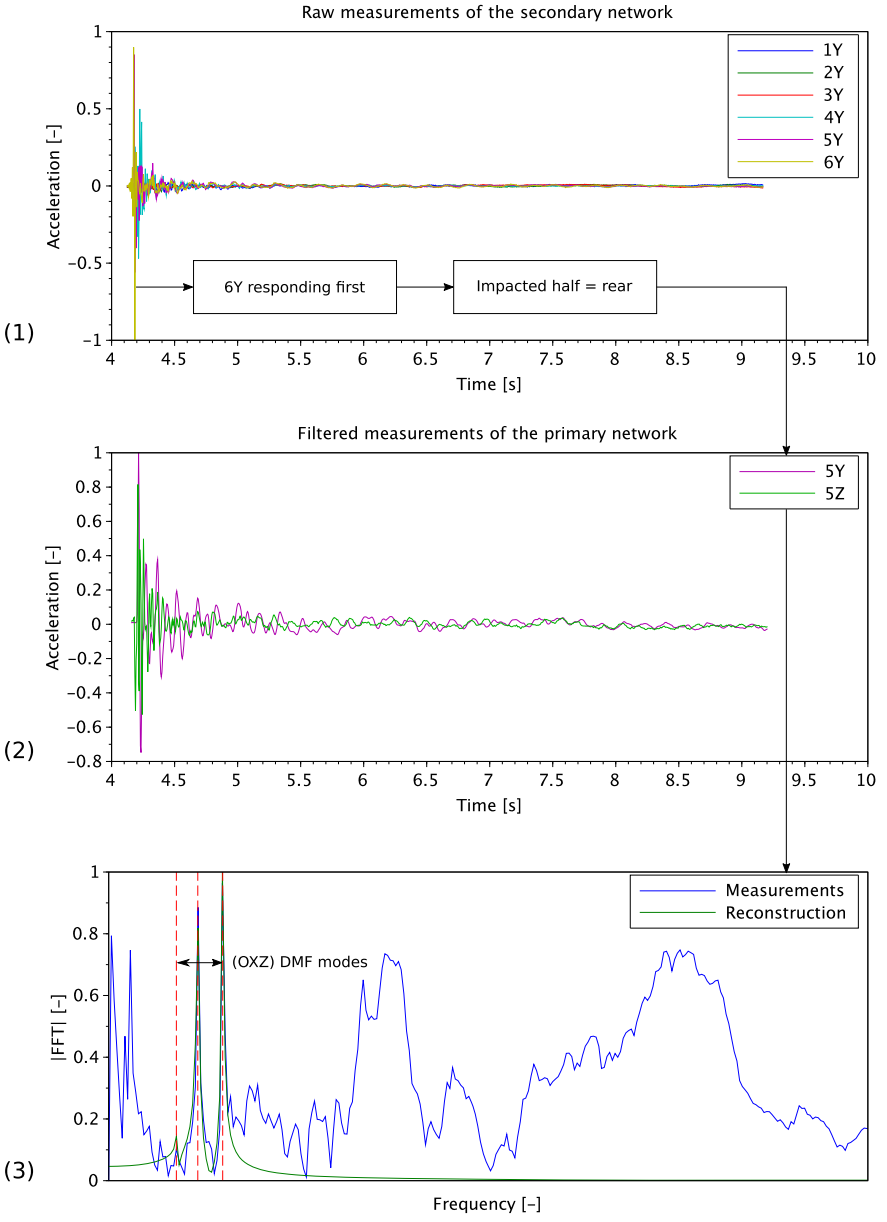

Figure 8. Illustration of the program flowchart for the impact applied at $x = 52$ m and $z = 5$ m (bottom right of the rear PAX door). (1) Detection of the impacted half. (2) Selection of rear primary sensor measurements. (3) Spectrum reconstruction of 5Z measurements with $(0XZ)$ DMF modes.

Second, it is observed that the localization error in the Z-direction is lower (≈0.7 m) than the mean localization error in the X-direction (≈1.6 m). This is because the axial localization is performed by using low-frequency mode shapes of the aircraft that slowly vary along the X-axis (see Appendix). The Z-coordinate of the impact point is estimated by another approach based on the estimation of the impact force direction.

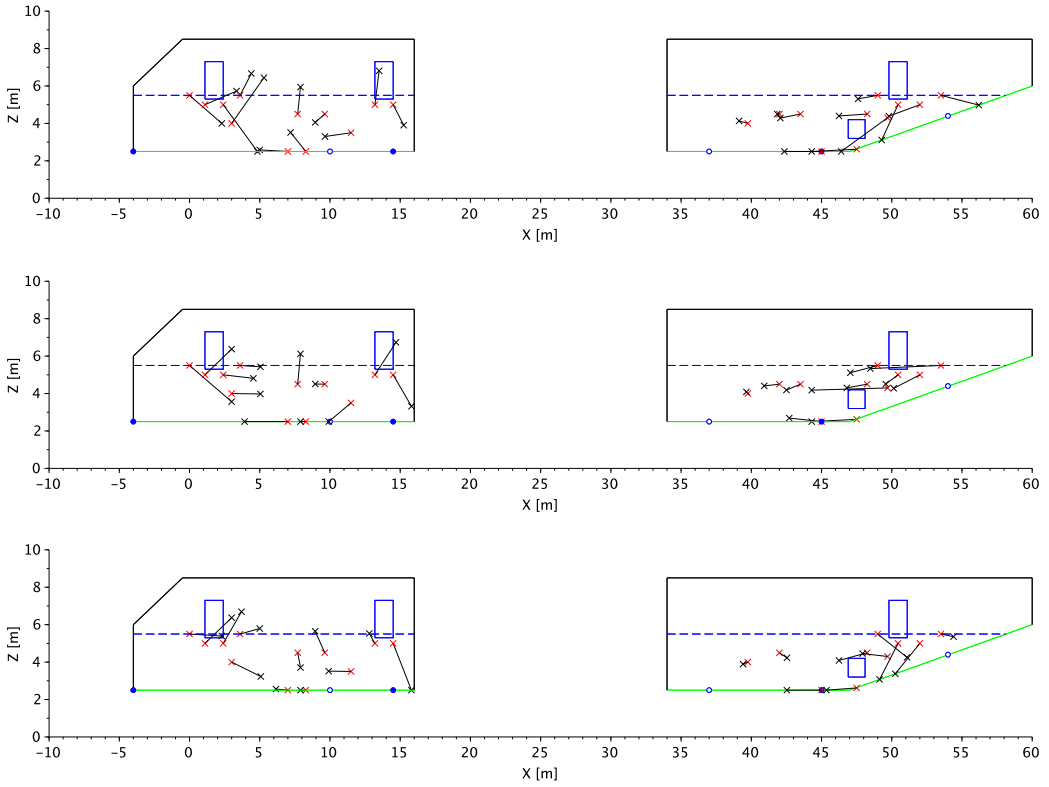

Figure 9. Localization maps with six accelerometers for the three series of impacts (one impact location removed from the third series because of invalid measurements). Red cross: true impact location; black cross: estimated impact location.

Table 2. Mean localization errors

	Front	Rear
X-axis	1.4 m	1.9 m
Z-axis	0.9 m	0.5 m
2D	1.8 m	2.0 m

The mean 2D localization error $e_{\text{loc}} \approx 2$ m is to be compared with a characteristic length L_c of the aircraft. The fuselage surface covered by the detection system is roughly half of a cylinder with a length of 46 m (by removing the central section) and a radius of 3 m. The diagonal of this unwrapped surface can be taken as the characteristic length, which leads to $L_c = 47$ m. Therefore the mean localization error with respect to the structure's dimensions is

$$e_{\text{loc}} / L_c \approx 4\%. \tag{26}$$

It is remarkable that relation (26) has also been observed for the metallic plate ($L_c = 55$ cm) and the composite stiffened panel ($L_c = 9.5$ m) studied in [27]. This localization barrier, or spatial resolution, can be seen as a consequence of using low-frequency mode shapes that slowly vary in space.

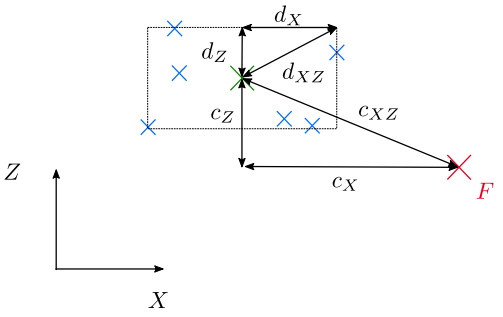

Figure 10. Definition of accuracy and robustness in 1D or 2D. The blue crosses are some impact point estimates $\hat{F}_i$ associated with the localization of impacts applied at the same point F (red cross). The dimensions d_X, d_Z, and d_{XZ} of the rectangle delimiting the estimates define the robustness in 1D or 2D. The distances c_X, c_Z, and c_{XZ} between the center of the rectangle (green cross) and the true impact point define the accuracy in 1D or 2D.

Table 3. Mean accuracy (c_X, c_Z, and c_{XZ}) and robustness (d_X, d_Z, and d_{XZ} in parentheses)

	Front	Rear
X-axis	1.4 m (0.4 m)	1.5 m (0.9 m)
Z-axis	0.7 m (0.8 m)	0.6 m (0.5 m)
2D	1.7 m (1 m)	1.7 m (1.3 m)

4.3. *Performance*

Accuracy and robustness are properties required for an impact localization technique. For instance, consider the localization results of numerous impacts applied at the same point $F = (x\ z)$ on some side of the fuselage. Each repetition is somehow different, which leads to a certain variability of the system parameters (impact energy, impact angle, ambient noise, etc.). The technique is said to be robust for localizing an impact applied in F if the diameter d_{XZ} of the set of all the estimates $\hat{F}_i$ is small. It is said to be accurate if the distance c_{XY} between the center of the set of the estimates and F is small. Figure 10 summarizes the definitions of accuracy and robustness (in 1D or in 2D).

For this study, three impacts have been applied per location to assess the mean accuracy and robustness of the proposed approach. Figure 11 illustrates representative localization scenarios that have been encountered. The localizations of the impacts applied at $x = 40$ m or $x = 42$ m are notably accurate and robust, while others are more accurate or robust depending on the considered axis (see the two impacts applied at the rear). Table 3 summarizes the mean 1D and 2D performance obtained during these tests. The results are satisfactory given the inputs used for this analysis (low sampling frequency measurements, ambient noise under outdoor conditions, and rough modal analysis of the aircraft).

Finally, Figure 12 represents the success rate for localizing an impact at a given proximity tolerance $\epsilon > 0$. It is remarkable that less than 50% of the impacts are localized within 2 m, but more than 90% are successfully localized within 3 m. This jump could be due to the spatial resolution evoked in the previous section due to the use of low-frequency mode shapes.

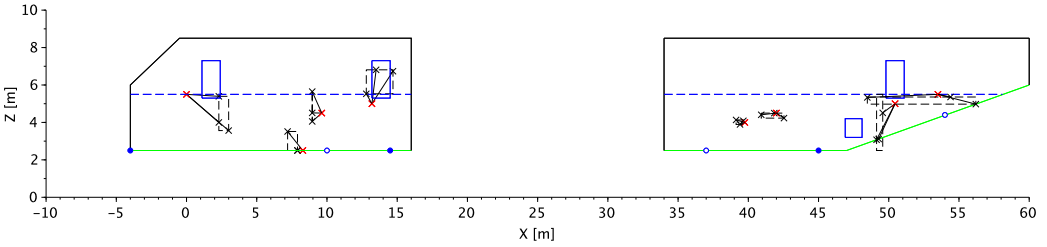

Figure 11. Accuracy and robustness depending on impact location.

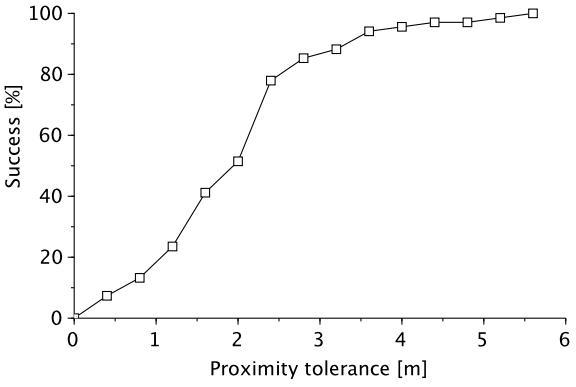

Figure 12. Localization success depending on proximity tolerance.

5. Conclusion

This paper presents a novel strategy for localizing impacts applied on a cylindrical composite fuselage. The proposed approach is efficient for quickly localizing the impacts by a small number of low sampling frequency sensors. This localization technique has been successfully validated under outdoor conditions on a 1:1 scale composite aircraft equipped with only six accelerometers. The localization performance obtained for the tested aircraft is consistent with the previous validations of the proposed technique on plate-like structures of much smaller dimensions. Hence this approach successfully scales up without requiring a significantly larger number of sensors.

This technique could be improved by optimizing the data fusion strategy between the sensor measurements of the primary network. In addition, one could extend it to the evaluation of the impact severity by using the estimation of impact intensity already computed in the proposed procedure. Future work should also be conducted regarding the automatic calibration of the modal model of the aircraft on ground to compensate for possible modal property shifts under operating conditions.

Appendix

An EMA of the tested aircraft on ground was performed by a tap-testing technique. The structure was equipped with 19 bi-axis accelerometers distributed along a line on the aircraft belly. An interpolation technique was used to increase the evaluation points to 82 (so that two successive evaluation points were roughly separated by a distance of 60 cm). Eleven mode shapes were

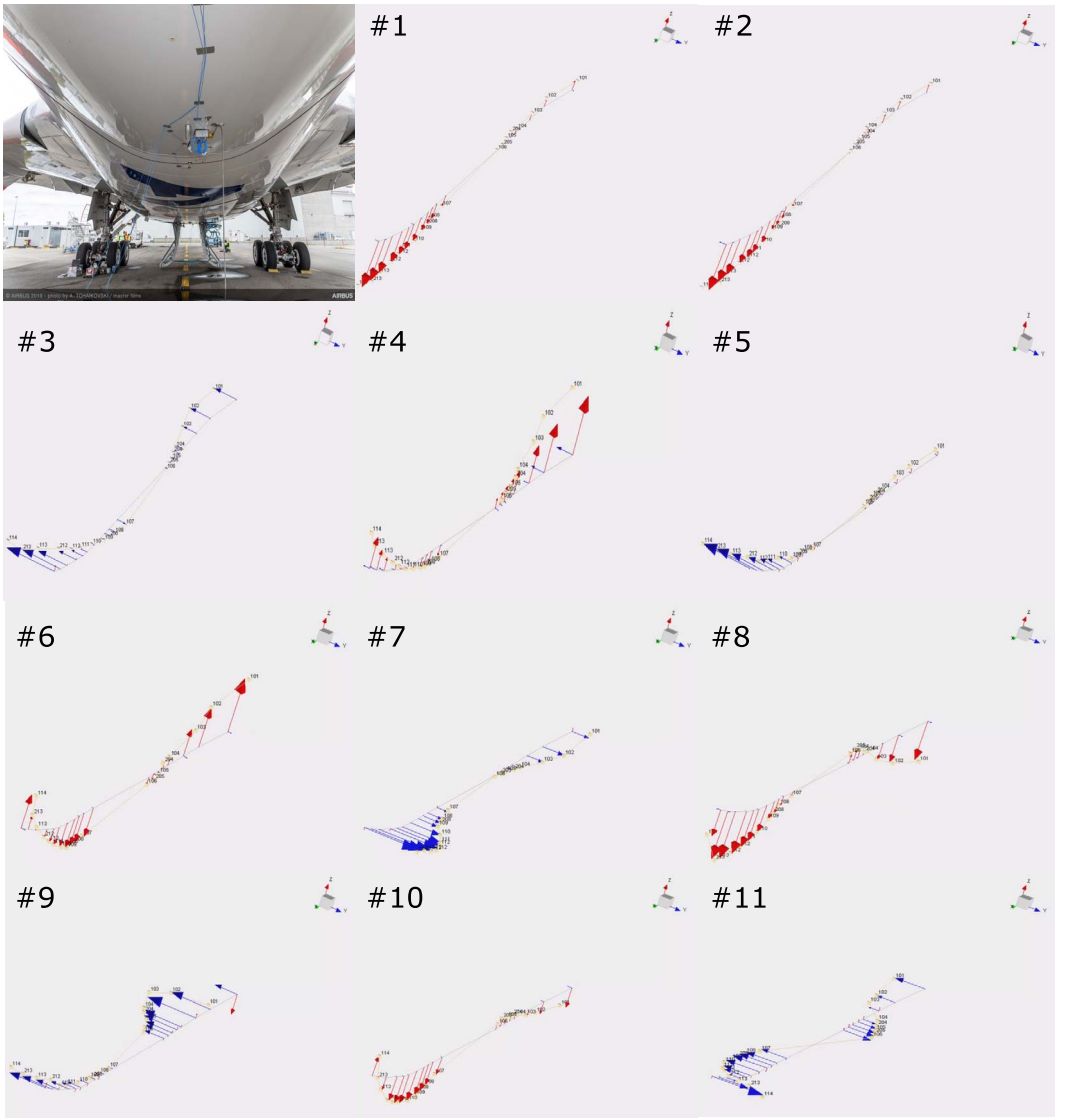

Figure 13. Eleven mode shapes extracted in the range 1 Hz–15 Hz during the EMA.

extracted between 1 Hz and 15 Hz (see Figure 13). However, the reciprocity plots suggested restricting the analysis to the frequency band 3 Hz–11 Hz (evidences of non-linear effects outside this range).

References

[1] W. Cantwell, J. Morton, "Comparison of the low and high velocity impact response of CFRP", *Composites* **20** (1989), no. 6, p. 545-551.

[2] S. Abrate, "Impact on laminated composite materials", *Appl. Mech. Rev.* **44** (1991), no. 4, p. 155-190.

[3] P. Kumar, B. Rai, "Delaminations of barely visible impact damage in CFRP laminates", *Compos. Struct.* **23** (1993), no. 4, p. 313-318.

[4] M. Rébillat, O. Hmad, F. Kadri, N. Mechbal, "Peaks Over Threshold–based detector design for structural health monitoring: application to aerospace structures", *Struct. Health Monit.* **17** (2018), no. 1, p. 91-107.

[5] G. Zhao, H. Hu, S. Li, L. Liu, K. Li, "Localization of impact on composite plates based on integrated wavelet transform and hybrid minimization algorithm", *Compos. Struct.* **176** (2017), p. 234-243.
[6] J. Achenbach, *Wave Propagation in Elastic Solids*, North-Holland Publishing Company, Amsterdam, 1973.
[7] R. Seydel, F.-K. Chang, "Impact identification of stiffened composite panels: I. System development", *Smart Mater. Struct.* **10** (2001), no. 2, p. 354-369.
[8] J. Frieden, J. Cugnoni, J. Botsis, T. Gmür, "Low energy impact damage monitoring of composites using dynamic strain signals from fbg sensors – Part I: Impact detection and localization", *Compos. Struct.* **94** (2012), p. 438-445.
[9] P. Shrestha, J.-H. Kim, Y. Park, C.-G. Kim, "Impact localization on composite wing using 1D array FBG sensor and RMS/correlation based reference database algorithm", *Compos. Struct.* **125** (2015), p. 159-169.
[10] Y. Zhong, J. Xiang, H. Gao, Y. Zhou, "Impact energy level assessment of composite structures using music-ann approach", *Struct. Control Health Monit.* **23** (2016), p. 825-837.
[11] A. Seno, Z. S. Khodaei, M. F. Aliabadi, "Passive sensing method for impact localisation in composite plates under simulated environmental and operational conditions", *Mech. Syst. Signal Process.* **129** (2019), p. 20-36.
[12] L. Vladislav, R. Zemcik, T. Kroupa, J. Bartosek, "Reconstruction of impact force on curved panel using piezoelectric sensors", *Proc. Eng.* **48** (2012), p. 367-374.
[13] A. El-Bakari, A. Khamlichi, E. Jacquelin, R. Dkiouak, "Assessing impact force localization by using a particle swarm optimization algorithm", *J. Sound Vib.* **333** (2014), no. 6, p. 1554-1561.
[14] Q. Li, Q. Lu, "Impact localization and identification under a constrained optimization scheme", *J. Sound Vib.* **366** (2016), p. 133-148.
[15] C. Chena, Y. Lia, F.-G. Yuanb, "Development of time-reversal method for impact source identification on plate structures", *Shock Vib.* **20** (2013), p. 561-573.
[16] F. Ciampa, M. Meo, "Impact localization on a composite tail rotor blade using an inverse filtering approach", *J. Intell. Mater. Syst. Struct.* **25** (2014), no. 15, p. 1950-1958.
[17] J. Park, S. Ha, F.-K. Chang, "Monitoring impact events using a system-identification method", *AIAA J.* **47** (2009), p. 2011-2021.
[18] A. Seno, Z. S. Khodaei, M. F. Aliabadi, "Partial least square/projection to latent structures (PLS) regression to estimate impact localization in structures", *Smart Mater. Struct.* **22** (2013), no. 2, article no. 025028.
[19] E. D. Niri, S. Salamone, "A probabilistic framework for acoustic emission source localization in plate-like structures", *Smart Mater. Struct.* **21** (2012), no. 3, article no. 035009.
[20] J. Zhu, S. C. M. Ho, D. Patil, N. Wang, R. Hirsch, G. Song, "Underwater pipeline impact localization using piezoceramic transducers", *Smart Mater. Struct.* **26** (2017), no. 10, article no. 107002.
[21] D. Goutaudier, D. Gendre, V. Kehr-Candille, R. Ohayon, "Single-sensor approach for impact localization and force reconstruction by using discriminating vibration modes", *Mech. Syst. Signal Process.* **138** (2020), article no. 106534.
[22] J. Doyle, *Wave Propagation in Structures*, Springer, New York, 1989.
[23] M. Géradin, D. J. Rixen, *Mechanical Vibrations - Theory and Application to Structural Dynamics*, 3rd ed., Wiley, 2015.
[24] P. Lubrina, S. Giclais, C. Stéphan, M. Boeswald, Y. Govers, N. Botargues, "AIRBUS A350 XWB GVT - State of the art techniques to perform a faster and better GVT Campaign", in *Topics in Modal Analysis II*, vol. 8, Springer International Publishing, 2014, p. 243-256.
[25] M. Böswald, D. Göge, U. Füllekrug, Y. Govers, "A review of experimental modal analysis methods with respect to their applicability to test data of large aircraft structures", in *Proc. of ISMA 2006, the Int. Conf. on Noise and Vibration Eng., Leuven, Belgium*, 01 2006, p. 2461-2481.
[26] M. Mitra, S. Gopalakrishnan, "Guided wave based structural health monitoring: a review", *Smart Mater. Struct.* **25** (2016), no. 5, article no. 053001.
[27] D. Goutaudier, "Impact identification technique for a structure with weakly damped and well-separated low frequency vibration modes", PhD Thesis, Conservatoire National des Arts et Métiers de Paris, 2019, https://tel.archives-ouvertes.fr/tel-02125320.
[28] G. DeFrancisci, "High energy wide area blunt impact on composite aircraft structures", PhD Thesis, University of California, San Diego, 2013, https://escholarship.org/uc/item/7fq9827j.
[29] E. Morteau-Rivet, V. Faivre, "Damage tolerant composite fuselage sizing, characterization of accidental damage threat", *Airbus Tech. Mag. FAST* **48** (2011), p. 10-16.